Salp Swarm Algorithm-Based Fractional Order PID Controller for Grid-Connected Hybrid Renewable Energy System

Anas Quteishat[1] iD, Mahmoud A. Younis[2], Arman Amini Badr[3],

Ali Khezerlou[4], Amin Safari[5]* iD

[1] Electrical Engineering Department, Faculty of Engineering Technology, Al Balqa Applied University, Al-Salt, Jordan.
[2] Department of Electrical and Computer Engineering, Sohar University, Sohar, Oman.
[3, 4, 5] Department of Electrical Engineering, Azarbaijan Shahid Madani University, Tabriz, Iran

Abstract— One of the most important tasks of sustainable energy is to store and keep natural resources while also developing practical solutions to environmental problems. The performance of renewable energy systems is significantly impacted by their control system. In order to model and control the system more efficiently, the fractional order PID (FOPID) controller - as a generalized version of the classical controller - employs fractional derivative-integral calculus. The design of an optimal FOPID controller for the grid-connected hybrid solid oxide fuel cell-wind turbine system is the primary objective of this research in addition to assessment of its dynamic stability. The proposed controller parameters are optimally scheduled using the Salp Swarm Algorithm (SSA), with the objective function that minimizes the absolute value of the error. The simulation results of the studied system subjected to various configurations and operating conditions are presented to demonstrate the effectiveness of the proposed control scheme, and a comparison of the FOPID controller with the PID controller has also been conducted. The simulation findings show that the effectiveness of the proposed SSA technique is based on criteria regarding the steady-state error, overshoot, as well as the settling time related to the power, speed, and delta deviations associated with the system under study.

Keywords— Fractional-order PID; Wind turbine; Solid oxide fuel cell; Salp swarm algorithm; Hybrid renewable energy system.

1.   INTRODUCTION

Currently, one of the main concerns in power generation is saving nonrenewable fossil fuels and using clean and inexpensive sources as network-connected power plants. The solid oxide fuel cell (SOFC) will play an influential role as one of the most useful and effective sources in power systems [1, 2]. In respect of the quick improvement of SOFC technology and wind turbines (WT), it is expected that the generation of considerable SOFCs and wind farms in connected-network mode will have a significant consequence on the present structure at an early date. Wind turbines can be utilized alone or in groups, and their technology and capacity continue to rapidly improve with the goal of realizing higher performances. On the other hand, when high-capacity renewable energy sources are in play, it is essential to analyze the stability of the system. The rapid increase in electricity consumption leads to the operation of power systems near their stability domain. Therefore, the effects of renewable electricity generation, such as large-sized SOFCs and WTs, on the security assessment and dynamic stability of the system have been investigated in the present study as an important subject for future integrated power systems.

Various models of integrated SOFC units in electrical power networks are presented in [3-9]. A mathematical Heffron-Philips model for SOFC, which is employed in a multi-machine system, is proposed in [3] to investigate the dynamic durability of the considered system. The particle swarm optimization technique is used to optimize the low-frequency oscillation damping by utilizing system stabilizers. In [4], several control methods are presented to get a minimum transient time for changing the output power level of a grid-connected SOFC. The action of a power plant in various operating states considering a new model for SOFC is introduced in [5]. A simplified model for micro-turbines and fuel cells is developed in [6] for slow-dynamic simulations. For optimal operation of the stack, a fuel cell model and a controlling approach are suggested in [7]. The grid-connected fuel cells are used to power electronic interfaces. Nonlinear dynamic modeling of a SOFC for small signal stability and transient analysis of distribution systems, including these resources, is presented in [8, 9]. The effects of fuel cell control methods on the stability enhancement of the overall system are investigated using a MATLAB-based toolbox. Measures and control strategies for SOFC-safe operation have been implemented to ensure stack temperature and voltage remain within safe and optimum parameters. A nonlinear controller was designed in [10] to ensure the SOFC follows the desired stack temperature and voltage, using dynamic compensation as its basis.

As the electrical output power of the double-fed induction generator (DFIG) is independent of speed, it is mostly used in variable-speed wind turbines [11]. Numerous studies have been done on this type of wind generation to develop its modeling and grid stability analysis [12-15]. In [12], a state space model of a DFIG-based wind turbine is proposed to evaluate the transient and small signal stability of the system. Particle swarm and teaching learning-based optimization techniques are used to devise an optimal PI controller for the suggested model. An algorithm based on the particle swarm is applied in [13] to find optimal coordinated control of multiple controllers for a wind turbine with DFIG. A new non-dominated sorting genetic algorithm-II optimization approach incorporating discrete Fourier transform is presented in [14] to improve the DFIG performance and provide a desirable stability margin. Ancillary controllers for a DFIG-based wind farm are provided in [15]. These controlling actions reinforce the voltage stability of the system as well as its frequency stability. In [16], the influence of system parameter variations on power network stabilizer parameters was studied by introducing a unified power flow controller and using support vector regression in order to damp out the small signal oscillations, thereby improving transient stability. In a study conducted by [17], a passivity-based bilinear PI controller was proposed for integrating superconducting magnetic energy storage devices into AC microgrids. The controller provides stability and robustness to the system when in operation, offering an asymptotic solution according to Lyapunov stability theory. The small signal stability of hybrid sustainable energy resource microgrids, including solar and wind generations, is discussed in [18, 19]. Few articles have investigated the effects of wind turbines and fuel cells on the stability of hybrid power systems. The hybrid systems integrated with fuel cells and wind turbines have been dynamically assessed in [20-22]. In [20, 21], dynamic modeling of considered isolated systems, including fuel cells and wind turbines, is presented in different conditions to determine expected transients and the output voltage variations. These systems can be effectively utilized in off-grid, remote areas. A new optimization algorithm is presented in [22] to achieve high efficiency for wind turbines under turbulent conditions by employing a fuel cell stack as a backup source for the hybrid system. The proposed technique is implemented for both

constant and variable loads. Also, in [23], an optimized controlling approach for a grid-connected microgrid containing solar and wind-fuel cell hybrid generation is presented to increase the dynamic stability of the power system. A combination of a radial basis function network-sliding mode and a modified general regression neural network control is used as the controlling approach, which is applied to deal with power inconsistences and uncertainties regarding the load and sustainable resources. A Heffron-Philips model for a low voltage microgrid, including a complementary stabilizer, is presented in [24]. The stabilizer aims to improve the stability of the microgrid consisting of PV, diesel machine, induction motor, and governor using an imperialist competitive algorithm to obtain optimal gains for the design. The authors in [25] introduce optimal stabilizers for low-frequency oscillation damping in a single-machine infinite-bus system encompassing a SOFC. The optimization process is implemented based on a PSO algorithm that optimizes the parameters of the employed stabilizers. In [26], a comprehensive mathematical model of a directly fed induction generator wind turbine with direct power control and an infinite bus system is described. It proposes a strategy to adjust the parameters of the wind turbine control system depending on the prevailing wind conditions, with particular regard to small signal stability. In [27], the effects of wind energy on the small signal stability of a power system were evaluated.

A fractional-order dragonfly algorithm was utilized in [28] to minimize the sum of squared errors between the output voltage of the empirical data and the obtained data for the unknown parameter identification of SOFC. In [29], a coordinated parameter optimization model of droop-based fast frequency controllers is proposed for the small signal rotor angle stability of DFIG. Also, violations of the control parameter constraints are handled by solving the proposed optimization model using a sensitivity-based method. In [30], an advanced nonlinear implicit dynamic model is presented, which includes a DC-DC converter, a lithium-ion battery, a PV array, and a SOFC. The optimal parameters of the droop controller would be determined using NSGA-II, a method that optimizes both transient efficiency and power tracking performance. In [31], a self-tuning controller based on PSO is presented to adapt the real power controller gains of a linearized model of an islanding system comprising an SG and DFIG for small signal stability analysis in real-time. In [32], a small-signal state-space model for grid-connected DFIG systems was established to deal with stability problems during asymmetric grid faults. Besides, a novel PS and NS current control reference optimization algorithm to suppress the oscillation of the system is proposed. The small signal dynamic response of a grid-connected SOFC system may be enhanced by adjusting its PI controller using a differential evolution (DE) algorithm, as demonstrated in [33]. The performance of the proposed algorithm was investigated in comparison with the PSO and IWO algorithms for different load disturbances for the time domain-based results.

Numerous studies have been carried out to create a damping controller for closed loop control systems. However, the existing methods require an extensive amount of time for implementation. Furthermore, the use of metaheuristic algorithms for controller design may not be as reliable due to the possibility of being stuck in a local optimum. Additionally, many metaheuristic-based approaches require various user-defined controlling parameters, and finely tuning these parameters to get the optimal solution is still a challenge. Along with conventional controllers such as PI, PID, and fuzzy, advanced controllers such as fractional order are gaining attention in this field due to their increased efficiency, and researchers need to focus more on researching the use of these advanced tools.

The authors ensured that the potential issues were addressed by introducing FOPID with the recent approach of SSA and installing it in a hybrid renewable energy system. This approach balances exploration and exploitation to prevent getting stuck in local optima. Additionally, it is simple to use and less affected by the parameters defined by users.

The major contributions of this paper are as follows:

- A dynamic analysis of a grid-connected hybrid wind-SOFC power system is introduced.
- An optimal FOPID is contributed and demonstrated to enhance the hybrid system stability and damp the oscillations.
- Optimal structuring of SSA-based FOPID is demonstrated.

In this paper, the introduction of a proposed algorithm is described in Section 2. The modeling and configuration of the system are presented in Section 3. Section 4 shows the improved Heffron-Philips model of the hybrid system. Finally, in Section 5, the dynamic responses of this model are presented, explained, and evaluated

2.   SALP SWARM ALGORITHM (SSA)

One of the new metaheuristic optimization algorithms that provides solutions to various optimization problems, including complex design problems, is SSA. Salps are sea animals that have opaque, barrel-shaped bodies. The formation of their bodies looks like jellyfish, and their behavior is similar to theirs. They move whenever water pushes them. A swarming attitude is the primary inspiration source for building SSA based on Salp's movement. Here, optimization problems are solved based on a primary model of Salp chains. SSA can solve single and multi-objective problems and gather the best solution faster than other heuristic algorithms [34].

Leader and followers denote two parts of the population, separated to achieve a mathematical formulation for the Salp chains. The leader is placed at the starting point of the chain, whereas the remaining Salps are located at other places and considered followers. Like other swarm optimization methods, the Salp position is considered in an N-dimensional space by searching where N is the number of problem variables. So, places of whole Salps are saved in a two-dimensional matrix named x. The principal purpose of Salp swarms is the food place which is called F. Eq. (1) represents updating the position of the leader:

$$X^1_j = \begin{cases} f_j + c_1\left(\left(ub_j - lb_j\right)c_2 + lb_j\right) & c_3 \geq 0 \\ f_j - c_1\left(\left(ub_j - lb_j\right)c_2 + lb_j\right) & c_3 < 0 \end{cases} \tag{1}$$

where, X^1_j shows the position of the first Salp (leader) in the jth dimension, lb_j and ub_j indicate the lower and upper bounds, respectively, and f_j is the position of the food source. c_1 as the main parameter of SSA could be evaluated utilizing Eq. (2) below. Also, c_2 and c_3 are random numbers that are generated uniformly between [0, 1].

Just, the leader of the Salp chain is allowed to set the locations that are related to the food place. The coefficient c_1 balances exploitation and exploration; indeed, it is the most critical parameter in SSA and is defined as:

$$c_1 = 2e^{-\left(\frac{4l}{L}\right)^2} \tag{2}$$

where, L refers to the largest number of iterations and l is the present iteration. If the next setting in the jth dimension must be towards negative or positive infinity, random numbers can dictate step size as well.

The following equations are used to set the place of the followers (Newton's law of motion):

$$x^i_j = \frac{1}{2} at^2 + v_0 t \tag{3}$$

where, $i \geq 2$, x^i_j shows the place of the ith follower Salp in the jth dimension, t shows the time, v_0 is the initial speed, and $a = \frac{v_{final}}{v_0}$ where, $v = \frac{x - x_o}{t}$.

Here, t shows the iteration number in optimization. The contrast between iterations is 1, so considering $v_0 = 0$, Eq. (3) can be arranged as follows:

$$X^i_j = \frac{1}{2}\left(x^i_j + x^{i-1}_j\right) \tag{4}$$

where $i \geq 2$ and x^i_j shows the position of the ith follower salp in the jth dimension. The salp chains can be simulated using Eqs. (1)-(4). Calculating the global optimum is the main goal for SSA. In the considered swarm model, followers track the leader, which moves toward the food source. If the global optimum replaces the food source, the chain automatically runs toward it. The flowchart of the Salp swarm optimization technique is illustrated in Fig. 1.
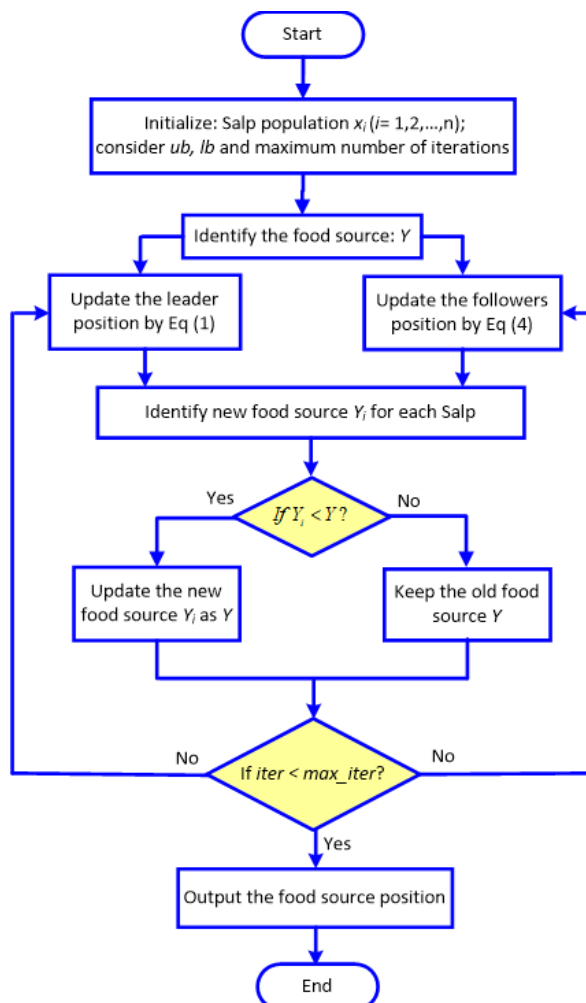

Fig. 1. Flowchart of the Salp swarm optimization technique.

The SSA initiates the optimization process by randomly setting multi-Salps and then evaluating the fitness of each Salp to identify the most fitness one. The best Salp is placed at variable f to be tracked by a chain of Salps.

For each dimension, Eqs. (2) and (4) update the sitting of the leading Salp and the sitting of the follower Slaps, respectively. Salp will regain its boundaries if it goes outside the search zone. SSA features can be expressed as:

- Identify the optimal Salp location as a food source variable and update that location during the optimization operation.
- Explore and exploit the search space around the optimal solution at each iteration through the leader Slap, updating its location according to food sources.
- Updating the positional relationship between follower Salps and guiding them to the leader Salp.
- Escaping from local optima due to slow motion of the follower Salp.
- Adaptively reduce c_1 as the main control parameter of SSA by increasing the number of iterations.
- Applying the SSA to resolving a solution to real optimization problems implies uncertain and complex search spaces.

3.   PROBLEM FORMULATION

3.1. Hybrid System Configuration

Fig. 2 shows the connection configuration of a SOFC generation unit and a wind turbine to a single-machine infinite-bus system. Where, x_s , x_{ts} , x_{tw} and x_t are the equivalent reactances for the transformers, transmission lines connected to the SOFC, synchronous generator, WT and grid, respectively. Also, V_b indicates the voltage of the infinite bus, V_t represents the terminal voltage of the synchronous generator, V_w denotes a wind generator's terminal voltage, and V_c is the bus voltage for the SOFC.
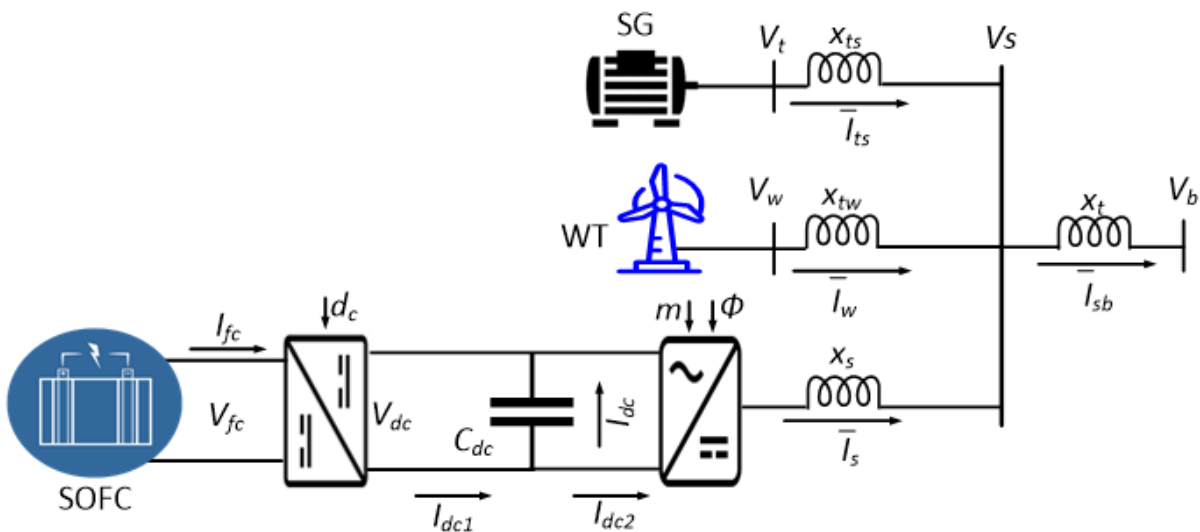

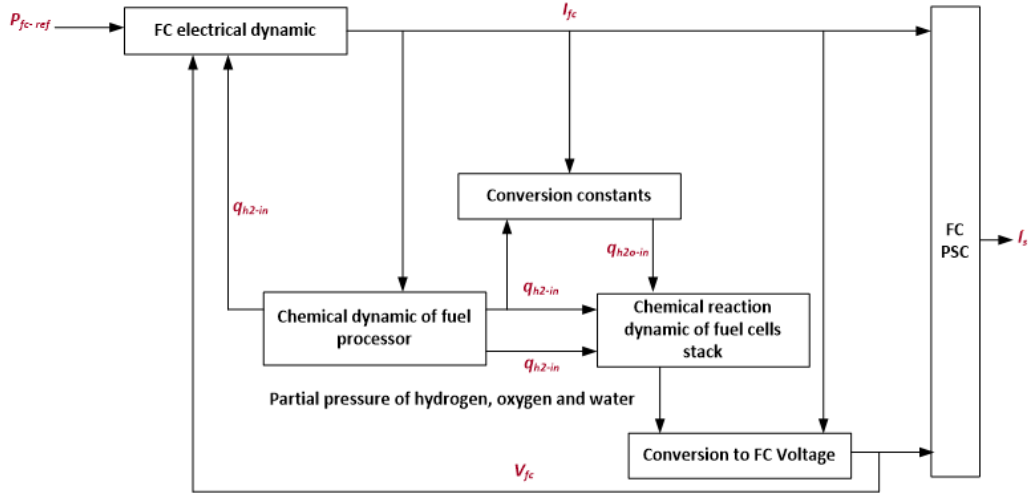Fig. 2. Connection configuration of the hybrid power system.

Fig. 3. Dynamic model of the SOFC.

Finally, I_s, I_w and I_{ts} refer to the currents of SOFC, WT and synchronous generator, respectively. The linearized and state space models of the SOFC based on the system given in Fig. 2 are more fully presented in [25].

3.2. Modeling the SOFC

Fig. 3 indicates the relevant dynamic block diagram of the SOFC generator [3-10]. The amount of power produced by a SOFC is proportional to the current flowing through it. The SOFC output power depends on current that passes through, and the output current must be controlled by the output power. Eq. (5) shows the dynamic model of the fuel cell with the time constant T_e. The output current is I_{fc} and I_{fc-ref} refers to the reference current of fuel cell in this first-order transfer function.

$$I_{fc} = \frac{1}{1+T_e\,s} I_{fc-ref} \tag{5}$$

I_{fc-ref} could be obtained using Eq. (6), where V_{fc} is the fuel cell output voltage and P_{fc-ref} denotes the reference power signal.

$$I_{fc-ref} = \left(\frac{P_{fc-ref}}{V_{fc}} \right) \tag{6}$$

The "chemical reaction dynamic" block in Fig. 3 represents the specific relation between the input fuel flow rate and the partial pressures of oxygen, hydrogen and water [25]. q_{o2-in} and q_{h2-in} are the input flows of oxygen and hydrogen, respectively.

According to Fig. 2, the power electronic interface of the SOFC generation unit includes two converters that connect SOFC to the grid. One of the converters is DC-DC, and the other is DC-AC. The output current control is realized with the DC-DC converter. So:

$$d_c = d_{c0} + \left(3 + \frac{1.57}{s} \right)\left(I_{fc-ref} - I_{fc} \right) \tag{7}$$

where, d_c and d_{c0} are duty cycles. The AC voltage of the DC-AC converter (V_c) at the output terminal of the SOFC unit can be written as [10]:

$$\bar{V}_c = m k V_{dc} \angle \psi \tag{8}$$

where V_{dc} is the voltage across the DC link, ψ is the angle deviation between V_{dc} and V_c, m denotes the modulation ratio and k depends on the converter's structure and is usually equal to 0.75. The modulation ratio controls the amplitude of the AC voltage.

The amount of power that the SOFC unit injects into the system can be quantified as follows:

$$P_{out} = i_{sd} m k V_{dc} \cos\psi + i_{sq} m k V_{dc} \sin\psi \tag{9}$$

where, v_{cd} and v_{cq} show the components of $\bar{V}_c$. The d and q components of $\bar{I}_s$ are i_{sd} and i_{sq} respectively. Also, Eqs. (8) and (9) can be used to get the DC-AC converter current:

$$I_{dc} = P_{fc} / V_{dc} - (i_{sd} m k \cos\psi + i_{sq} m k \sin\psi) \tag{10}$$

Moreover, the dynamic relation between voltage (V_{dc}) and current (I_{dc}) of the capacitor (C_{dc}) is presented as follows:

$$\dot{V}_{dc} = \frac{1}{C_{dc}} I_{dc} \tag{11}$$

The voltage controller stabilizes the voltage of the DC capacitor at a constant level.

3.3. Modeling the DFIG

It is common to study the dynamic behavior of a double-fed induction generator, converting the three-phase variables of the machine into a *d-q* frame as a rotating frame. Furthermore, in the stability analysis of this type of machine, a voltage source connected to the transient impedance can be applied [35]. The two-axis model for DFIG is defined based on a set of differential-algebraic equations. Therefore, the DFIG model could be expressed as [36]:

$$
\begin{bmatrix} \dfrac{dE'_d}{dt} \\[2mm] \dfrac{dE'_q}{dt} \end{bmatrix} = \frac{1}{T_0}
\begin{bmatrix} -\left(1 + x'\dfrac{x_s - x'}{|Z'|^2}\right) & s\omega_s T_0 + R_s \dfrac{x_s - x'}{|Z'|^2} \\[3mm] -\left(s\omega_s T_0 + R_s \dfrac{x_s - x'}{|Z'|^2}\right) & -\left(1 + x'\dfrac{x_s - x'}{|Z'|^2}\right) \end{bmatrix}
\begin{bmatrix} E'_d \\[2mm] E'_q \end{bmatrix}
$$
$$
+ \frac{1}{T_0}
\begin{bmatrix} x'\dfrac{x_s - x'}{|Z'|^2} & R_s \dfrac{x_s - x'}{|Z'|^2} & 0 & -\omega_s T_0 \dfrac{x_m}{x_r} \\[3mm] R_s \dfrac{x_s - x'}{|Z'|^2} & x'\dfrac{x_s - x'}{|Z'|^2} & \omega_s T_0 \dfrac{x_m}{x_r} & 0 \end{bmatrix}
\begin{bmatrix} v_{ds} \\ v_{qs} \\ v_{dr} \\ v_{qr} \end{bmatrix} \tag{12}
$$

$$
\bar{i}_s = \begin{bmatrix} i_{ds} \\ i_{qs} \end{bmatrix} = \frac{\bar{E}' - \bar{v}_s}{jx'} = \frac{1}{x}\left(\begin{bmatrix} -v_{qs} \\ v_{ds} \end{bmatrix} - \begin{bmatrix} -E'_q \\ E'_d \end{bmatrix}\right) \tag{13}
$$

3.4. SOFC and WT Integration with the Power System

Regarding the schematic diagram of Fig. 2, the system voltage formulations are given by Eqs. (14) and (15):

$$V_t + V_c + V_w = 3V_s + jx_{ts} I_{ts} + jx_s I_s + jx_w I_w \tag{14}$$

$$V_s - V_b = jx_t \left(I_{ts} + I_s + I_w \right) \tag{15}$$

Using Eqs. (14) and (15) in the *d-q* reference frame, the following equations could be obtained:

$$R_1 \begin{bmatrix} i_{tsq} \\ i_{sq} \\ i_{wq} \end{bmatrix} = \begin{bmatrix} V_b \sin\delta - V_c \cos\psi \\ V_b \sin\delta - V_{dw} \\ V_b \sin\delta \end{bmatrix} \tag{16}$$

$$R_2 \begin{bmatrix} i_{tsd} \\ i_{sd} \\ i_{wd} \end{bmatrix} = \begin{bmatrix} V_c \sin\psi - V_b \cos\delta \\ V_{qw} - V_b \cos\delta \\ E_q' - V_b \cos\delta \end{bmatrix} \tag{17}$$

where R_1 and R_2 are given in Appendix A. In this way, the proposed model of Fig. 2 is obtained.

3.5. Model Linearization

Considering small-signal linearization theory, From Eq. (8), it can be written that $\Delta V_c = k(m_0 \Delta V_{dc} + V_{dc0} \Delta m)$. Linearizing Eqs. (16) and (17) leads to:

$$\begin{bmatrix} \Delta i_{tsq} \\ \Delta i_{sq} \\ \Delta i_{wq} \end{bmatrix} = R_1^{-1} \begin{bmatrix} V_b \cos\delta_0 & 0 & -k\cos\psi_0\, m_0 & -k\cos\psi_0 V_{dc0} & V_{c0}\sin\psi_0 & 0 & 0 & 0 & 0 \\ V_b \cos\delta_0 & 0 & 0 & 0 & 0 & 0 & -x_s' & -1 & 0 \\ V_b \cos\delta_0 & 0 & 0 & 0 & 0 & 0 & 0 & 0 & 0 \end{bmatrix} X \tag{18}$$

$$\begin{bmatrix} \Delta i_{tsd} \\ \Delta i_{sd} \\ \Delta i_{wd} \end{bmatrix} = R_2^{-1} \begin{bmatrix} V_b \sin\delta_0 & 0 & k\sin\psi_0\, m_0 & k\sin\psi_0 V_{dc0} & V_{c0}\cos\psi_0 & 0 & 0 & 0 & 0 \\ V_b \sin\delta_0 & 0 & 0 & 0 & 0 & -x_s' & 0 & 0 & 1 \\ V_b \sin\delta_0 & 1 & 0 & 0 & 0 & 0 & 0 & 0 & 0 \end{bmatrix} X \tag{19}$$

where, $X = \begin{bmatrix} \Delta\delta & \Delta E_q' & \Delta V_{dc} & \Delta m & \Delta\psi & \Delta i_{wds} & \Delta i_{wqs} & \Delta e_d' & \Delta e_q' \end{bmatrix}^T$.

As SOFC equations will be linearized, Eq. (11) will be as follows:

$$\Delta \dot{V}_{dc} = -\frac{1}{C_{dc}} \left(\left(\frac{P_{sofc0}}{V_{dc0}^2}\right) \Delta V_{dc} + a_1 \Delta i_{sd} + a_2 \Delta i_{sq} + a_3 \Delta m + a_4 \Delta\psi \right) \tag{20}$$

Regarding Eqs. (8), (14) and (15), V_s could be linearized as:

$$\Delta V_s = B_1 \Delta\delta + B_2 \Delta E_q' + B_{dc} \Delta V_{dc} + B_3 \Delta m + B_4 \Delta\psi + B_5 \Delta i_{wds} + B_6 \Delta i_{wqs} + B_7 \Delta e_d' + B_8 \Delta e_q' \tag{21}$$

Based on the synchronous generator model of [37] and considering Eqs. (18) to (21), the following equation can be obtained:

$$\begin{bmatrix} \Delta P_t \\ \Delta E_q \\ \Delta V_t \end{bmatrix} = \begin{bmatrix} K_1 & K_2 & K_{pdc} & K_{pm} & K_{p\psi} & K_{pds} & K_{pqs} & K_{ped} & K_{peq} \\ K_3 & K_4 & K_{qdc} & K_{qm} & K_{q\psi} & K_{qds} & K_{qqs} & K_{qed} & K_{qeq} \\ K_5 & K_6 & K_{vdc} & K_{vm} & K_{v\psi} & K_{vds} & K_{vqs} & K_{ved} & K_{veq} \end{bmatrix} X \tag{22}$$

K coefficients are linearization constants [11]. As a result, Fig. 4 shows an adopted Heffron-Phillips model of a hybrid power system with an optimal controller. The electromechanical response of a synchronous generator is affected by SOFC and WT power

plants by K_p coefficients directly. Moreover, the influences of WT and SOFC on the field channel of a generator are depicted by both K_q and K_v parameters.
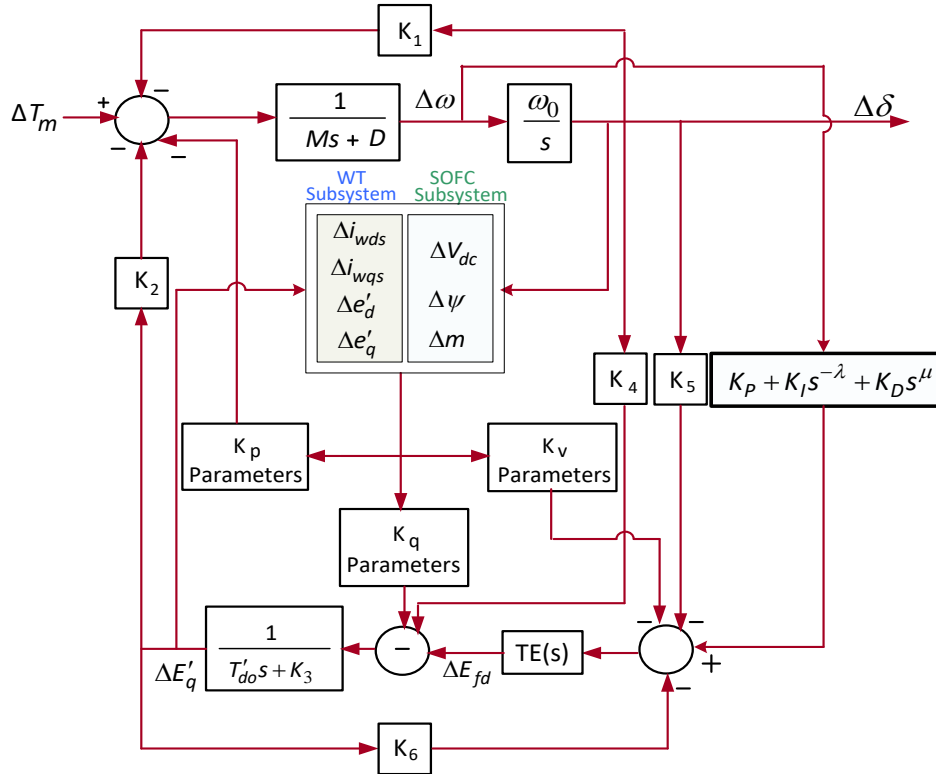

Fig. 4. Adapted Heffron-Phillips model of the hybrid system.

According to Fig. 4, the SOFC subsystem output variables are $\Delta m, \Delta V_{dc}$, and $\Delta \psi$, and the relation between input and output variables of the SOFC subsystem is made by the coefficients of the three blocks, obtained by linearizing the SOFC equations. The voltage behind the transient impedance and the wind turbine current are the output variables of this subsystem.

4.   SSA-BASED FOPID CONTROLLER DESIGN

To change the performance and endurance of the PID control system, the development of a PID controller, which can be called an FOPID controller, was proposed by Podlubny. PID controllers are frequently utilized in industry to optimize a system's transient and steady-state performance. These controllers are referred to be integer order or classic controllers. The fractional derivative-integral calculus is used by the FOPID controller, which is an extended version of the conventional PID controller. Beyond the parameters of a standard PID controller, the FOPID controller contains two more parameters. This extension of conventional PID controllers gives the system more robustness and adaptability. When compared to conventional PID controllers, FOPID controllers have the following advantages: reduced steady-state error, reduced oscillation and overshoot, improved response time, robustness to changes in the controlled system's parameters, and insensitivity to disruptive events are all advantages [38]. FOPID controllers can be an effective choice in power systems due to their flexibility and durability. Eq. (23) represents the transfer function of the FOPID controller [39]:

$$U_{PI^\lambda D^\mu}(s) = (K_P + K_I s^{-\lambda} + K_D s^\mu)\Delta\omega \tag{23}$$

One of the essential goals of the FOPID controller tuning investigations was to verify the significant improvement in controller flexibility and endurance specifications. K_P, K_I, K_D are the proportional, integral, and differential constants and μ and λ are fractional order derivative and integral elements for the design of FOPID controller, respectively. For $\lambda = \mu = 1$, classical PID controller, $\lambda = 1$, $\mu = 0$, PI controller and $\lambda = 0$, $\mu = 1$, PD controller can be written. Fig. 5 illustrates the types of classical PID controllers and denotes that they are a special case of FOPID controllers.
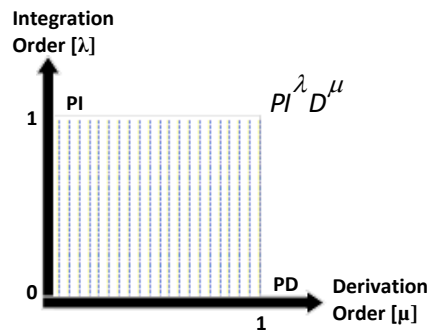

Fig. 5. Scheme of FOPID controllers.

One of the objectives of the controller is to enhance the damping of the critical modes to an admissible level. So, the proposed controller must have acceptable performance under different operating conditions while increasing the damping factor of the system-critical modes as an essential objective. The global optimum value of the objective function is found by SSA, and this algorithm improves the optimization results by selecting an optimal combination of FOPID gains for the damping controller. The whole of this process is a complex optimization problem. The objective function in this paper is to move eigenvalues to the left side of the imaginary axis and minimize the error signal using integral absolute error (IAE) and integral squared error (ISE) as indices for performance. To minimize the value of the objective function, the SSA has been applied to the system, which can be shown as follows:

$$F = W_1 \times \max\left(\sigma_i\right) + W_2 \times IAE + W_3 \times ISE \qquad i = 1, 2, 3, ..., N \qquad (24)$$

$$IAE = \int_0^{tsim} \left|e\left(t\right)\right| dt \qquad (25)$$

$$ISE = \int_0^{tsim} e\left(t\right)^2 dt \qquad (26)$$

where, σ and *tsim* are the real of eigenvalues, and whole simulation time, respectively. *N* is the total number of the eigenvalues and W_1, W_2 and W_3 are the weighting factor.

In the optimal controlling process, IAE and ISE show a complete performance criterion for the design of the controller and let it regulate the exchange between steady-state output error and controlled speed, which will improve the system dynamic action to a great extent. The SSA algorithm has been proposed as an efficient means of determining the top-performing settings for FOPID controllers while simultaneously offering superior exploration and exploitation capabilities. As seen in Fig. 6, the proposed SSA-FOPID Controller approach for controlling SG speed is depicted through a block diagram

To improve the five parameters of the FOPID controller, they are transformed into a salp population to be worked on by the proposed algorithm. This salp population is expressed as

a real number for each individual salp. The salps are optimized by undergoing the SSA, a procedure that allows them to reach an optimal state and minimize the value of a designated objective function. The initial population for the proposed scheme is made up of randomly generated salps and is of a certain size. Following that, the objective function in Eq. (24) is computed for each salp. The salps are then sent back to the optimization module to be adjusted for the following iteration. At the end of the optimization process, the salp with the lowest objective function value is identified as generating optimal FOPID parameters.
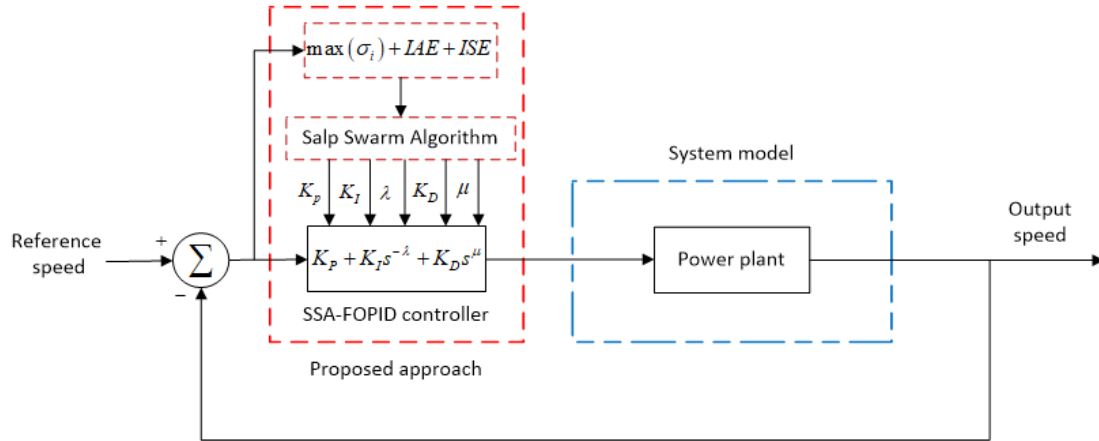

Fig. 6. SG speed control with SSA-FOPID controller.

By combining the objective function and WADC parameter constraints, an optimization model is developed that has the aim of minimizing *F* subject to:

$$K_P^{\min} \le K_P \le K_P^{\max}$$

$$K_I^{\min} \le K_I \le K_I^{\max}$$

$$K_D^{\min} \le K_D \le K_D^{\max}$$

$$\lambda^{\min} \le \lambda \le \lambda^{\max}$$

$$\mu^{\min} \le \mu \le \mu^{\max}$$

where, min and max refer to the minimum and maximum bounds of the parameters. The lower and upper limits of SSA parameters for the FOPID controller have been illustrated in Table 1. The following SSA parameters are used for the optimal design of the controller in the simulation process:

- Number of search agents = 10
- Number of maximum iterations = 8

The objective of the optimization problem is to find the best global optimum values of the parameters, which are given in Table 2.

Table 1. Upper and lower limits of the controller.

Parameters	K_P	K_I	K_D	λ	μ
Lower bound	35	5	3	0.5	0.6
Upper bound	50	15	5	0.7	0.8

Table 2. Optimum values of the FOPID controller.

Parameters	K_P	K_I	K_D	λ	μ
Optimal values	44.7778	7.1478	4.3703	0.62246	0.73569

5.   SIMULATION RESULTS AND PERFORMANCE EVALUATION

Three scenarios are investigated to study the small signal modeling of the SOFC and WT based system and show the effectiveness of the FOPID controller. Each scenario compares different parameters of the proposed system with a PID controller. A computer program was written in MATLAB for the proposed controller tuning process. The program ran on a 2.20 GHz Intel Core i7 processor with 6 GB of RAM. In order to get the most out of controller gain, it is important to set it at a certain level. If the gain is set too low or too high, there may be undesirable consequences. To ensure the best results, keep the optimizer's search space within upper and lower bounds as outlined in Table 1. This limited search space ensures that the computational time required by the optimizer is reduced. According to the results, the FOPID controller-based SSA could be used as one of the practical and helpful methods to enhance system damping thus reducing the overshoot of the system.

5.1.   Time-domain Simulation

Scenario 1: In this scenario, the result of the studied system is compared with PID simultaneously. Here, X_t equals to 1, 0.5 and 0.1 for the weak and strong grids [11]. It seems that when the system is connected to the FOPID controller, the output signals have better performance than those from the PID controller. The power deviation in Fig. 7 shows that both controllers have the same overshoot range, but the settling time of the FOPID controller is better than that of the PID controller.
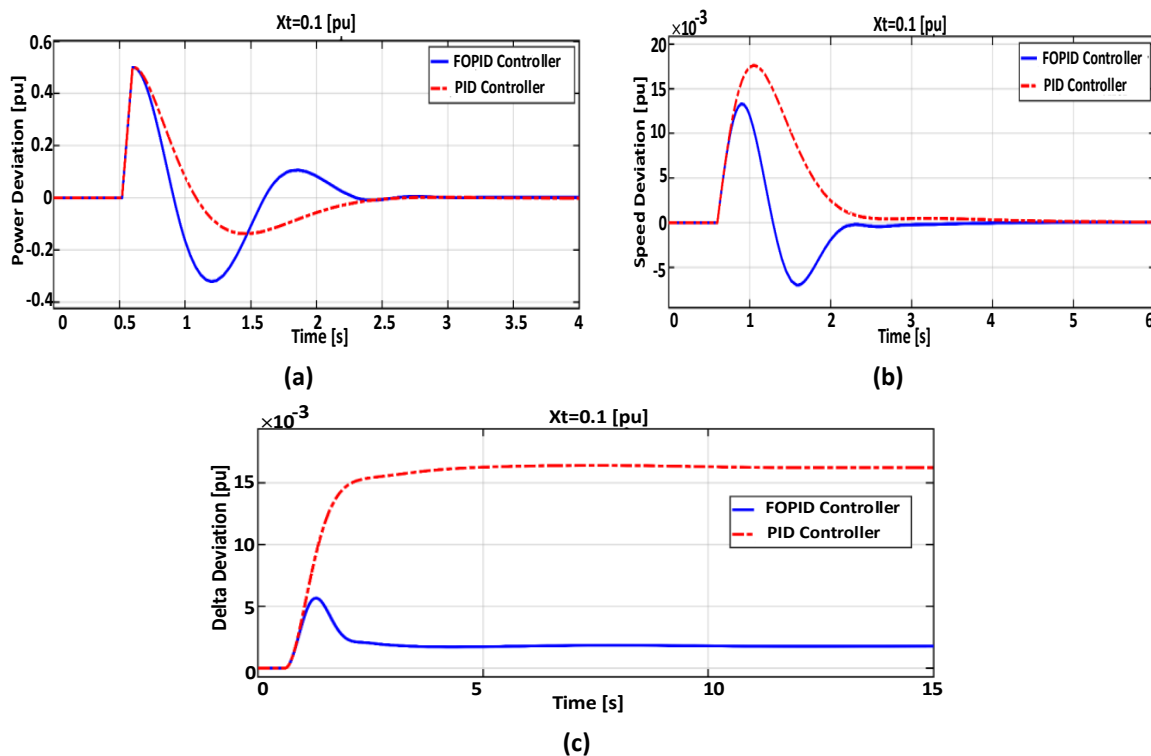

Fig. 7. Output signals of the system in scenario 1 by considering X_t = 0.1: a) power deviation; b) speed deviation; c) delta deviation.

For the speed deviation in the presence of the FOPID controller, the overshoot amplitude and settling time are 0.0135 per unit and 3.11 seconds, respectively. These values for the PID controller are 0.0184 per unit and 5 seconds. Also, it can be seen from the delta deviation that the amplitude and settling time with the application of the FOPID controller are much less

than when the PID controller is applied. In this way, it can be seen in Figs. 8 and 9 that by increasing X_t, the settling time and the overshoot by applying the FOPID controller has better performance and dynamic response compared to the PID controller.
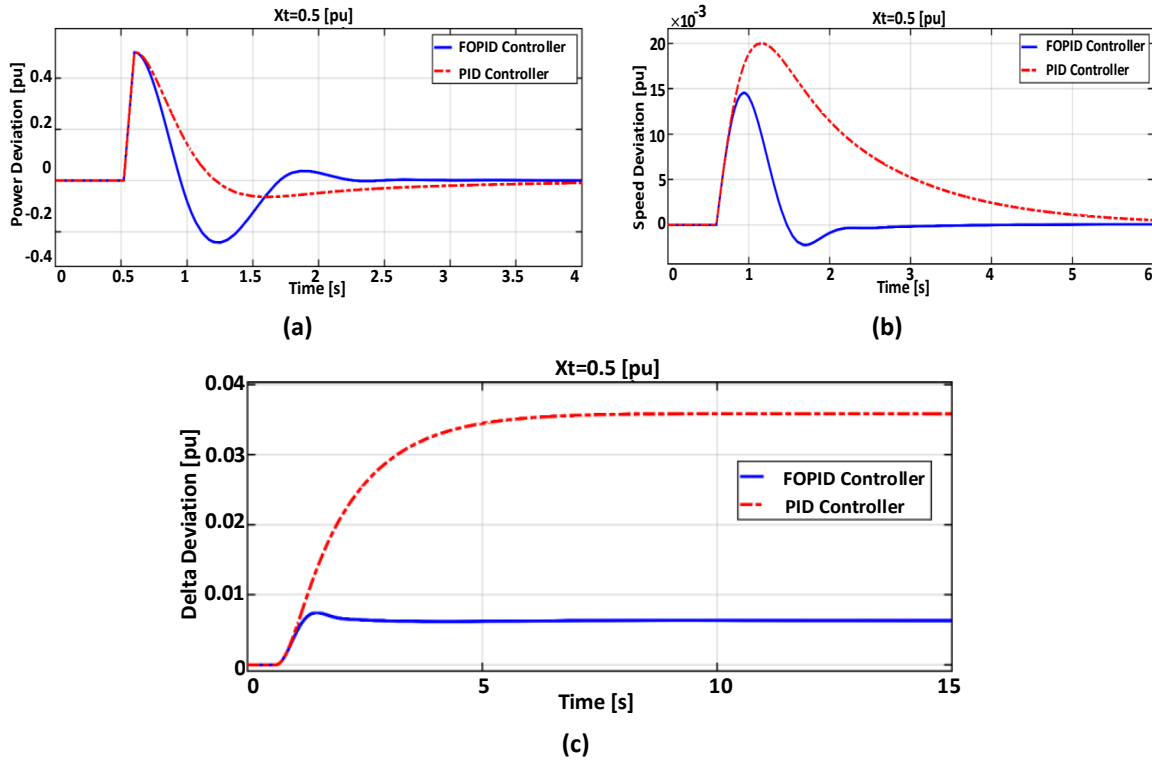

(a)

(b)

(c)

Fig. 8. Output signals of the system in scenario 1 by considering X_t = 0.5: a) power deviation; b) speed deviation; c) delta deviation.
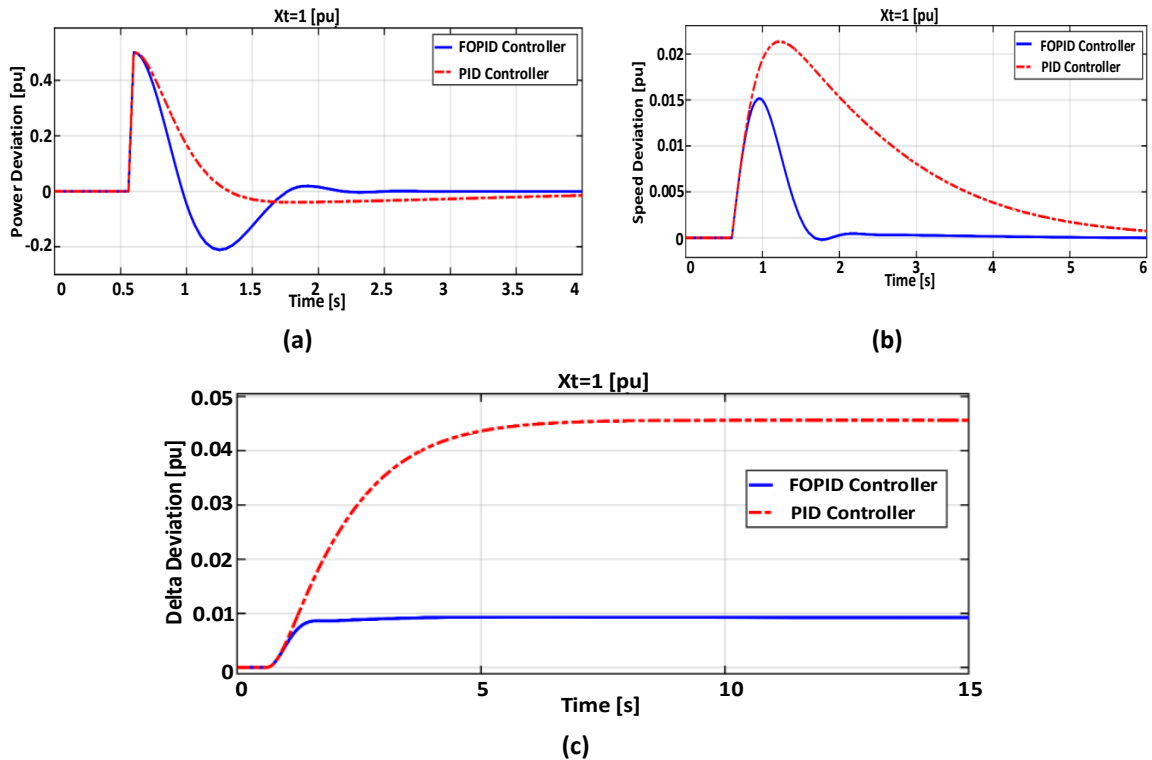

(a)

(b)

(c)

Fig. 9. Output signals of the system in scenario 1 by considering X_t = 1: a) power deviation; b) speed deviation; c) delta deviation.

As a result, when the system is connected to the FOPID controller, the overshot is decreased, and the settling time of the system becomes shorter.

Scenario 2: In this scenario, the effect of the proposed controller on the dynamic response of the hybrid system for different value of fuel cell voltage angle (ψ) is illustrated, in which the fuel cell voltage angle equals to 30, 70 and 100. According to Fig. 10, it can be seen that the overshoot amplitude for speed deviation is 0.0144 per unit while the system is connected to the FOPID controller, and the settling time, in this case, is 2.78 seconds. Besides, for the state in which the system is connected to the PID controller, the overshoot amplitude is 0.0188 per unit, and the settling time is more than 6 seconds.

Also, from Fig. 10, it can be concluded that in the presence of the FOPID controller, speed, and delta deviation have a grossly marked better performance compared to the PID controller. However, in favor of the PID approach we get better undershoot in the case of power deviation as evident by the power deviation graphs.

In the same way, the output signal of the system is illustrated in Figs. 11 and 12 for ψ = 70, 100. According to the results, changes in the value of ψ can cause system instability or raise the small signal stability margin of the system.
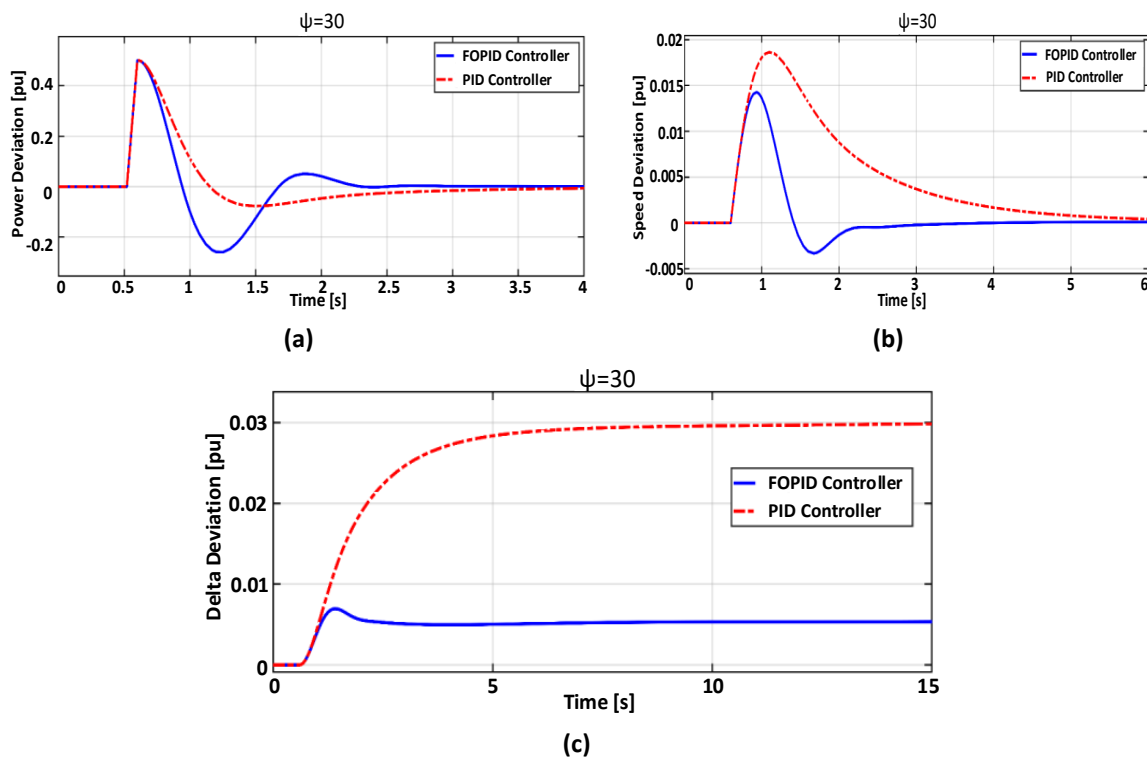

Fig. 10. Output signals of the system in scenario 2 by considering Ψ = 30: a) power deviation; b) speed deviation; c) delta deviation.

Scenario 3: In this scenario, the effect of the proposed FOPID controller on the dynamic response of the hybrid system for different values of step changes in terminal voltage has been illustrated. In which the step change value of terminal voltage is equal to 0.1, 0.3 and 0.5. According to Figs. 13-15, the power deviations in the presence of the FOPID controller have a lower settling time than the PID controller. Also, for speed deviations, the proposed controller has less overshoot amplitude and less settling time than the PID controller.

The values for the overshoot amplitude in the presence of the FOPID controller are equal to 0.0135, 0.0111 and 0.0105 per unit and for the PID controller, they are equal to 0.0184, 0.0133

and 0.0111 per unit. Also, the settling time of the proposed controller is equal to 4.32, 4.5 and 2.5 seconds, which is far less compared to the settling time of the PID controller, which is more than 6 seconds. According to Figs. 13-15, the FOPID controller greatly improves system stability. As a plus for the PID controller, in all three scenarios, the undershoot is smaller when it come the power deviation. An exception is demonstrated in the case where $V_t = 0.3$ pu as in Fig 14, where FOPID regains its superiority. As can be seen, output signals with SSA-tuned FOPID controllers have less settling time and overshoot for different voltage terminals.
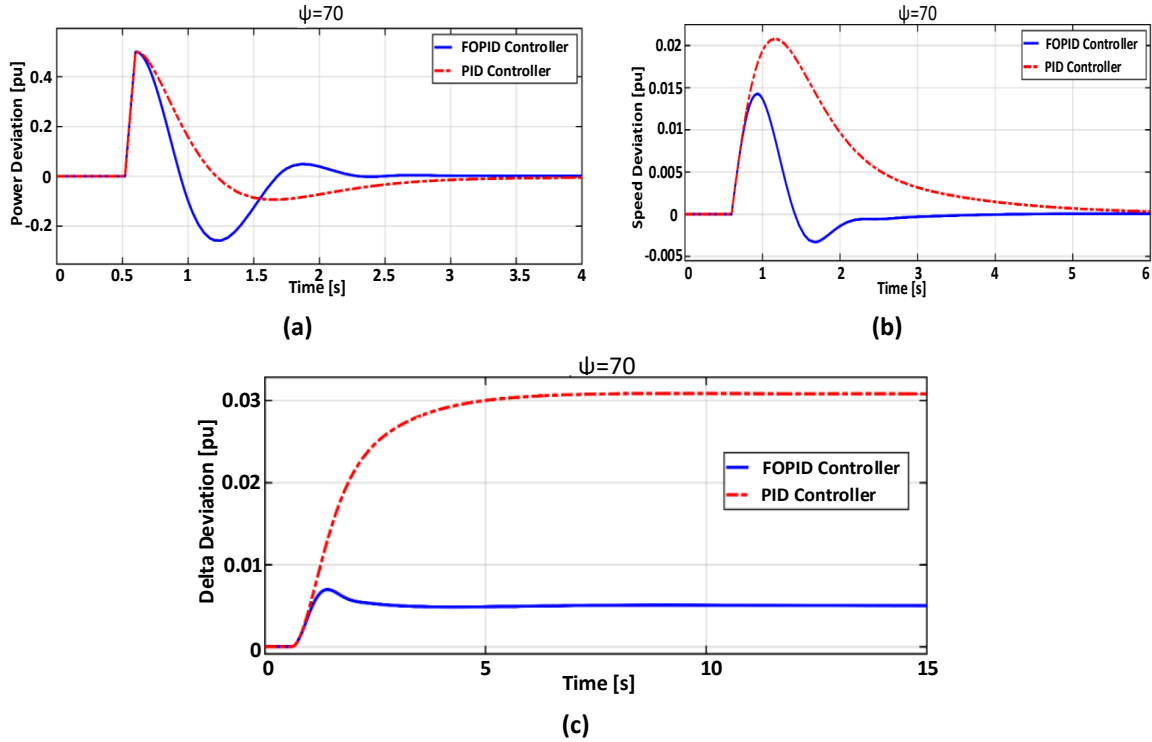

(a)   (b)

(c)

Fig. 11. Output signals of the system in scenario 2 by considering $\Psi = 70$: a) power deviation; b) speed deviation; c) delta deviation.

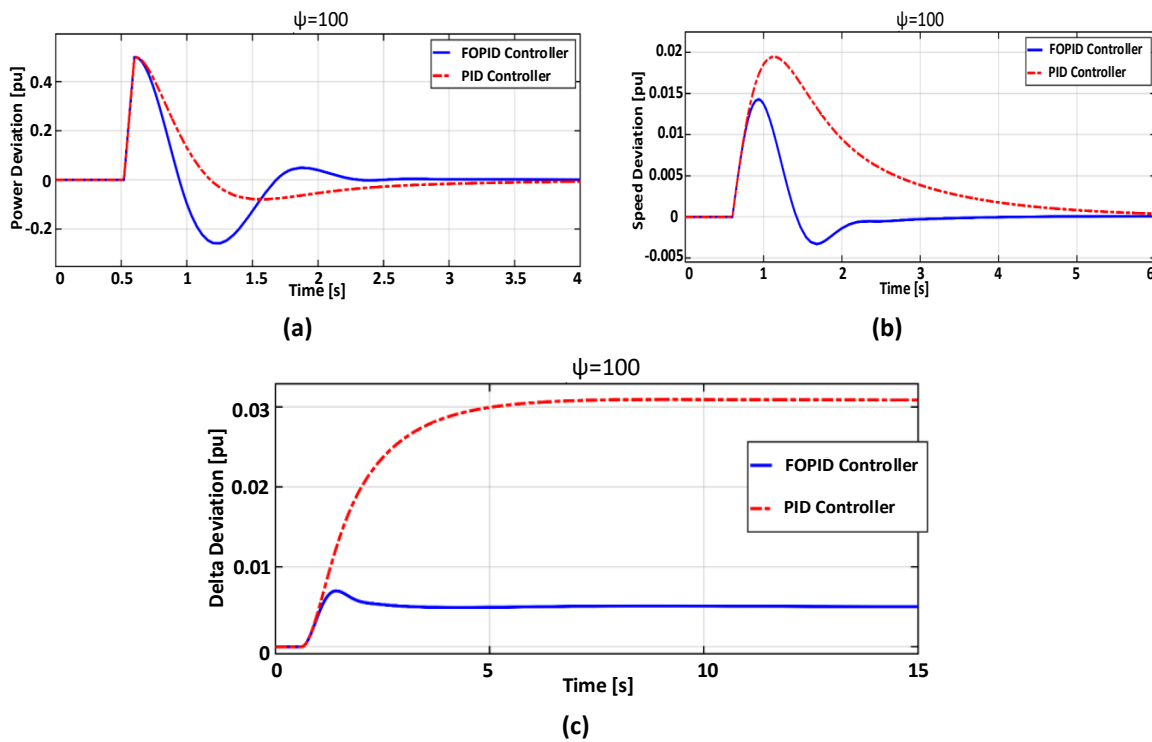(a)   (b)

(c)

Fig. 12. Output signals of the system in scenario 2 by considering $\Psi = 100$: a) power deviation; b) speed deviation; c) delta deviation.
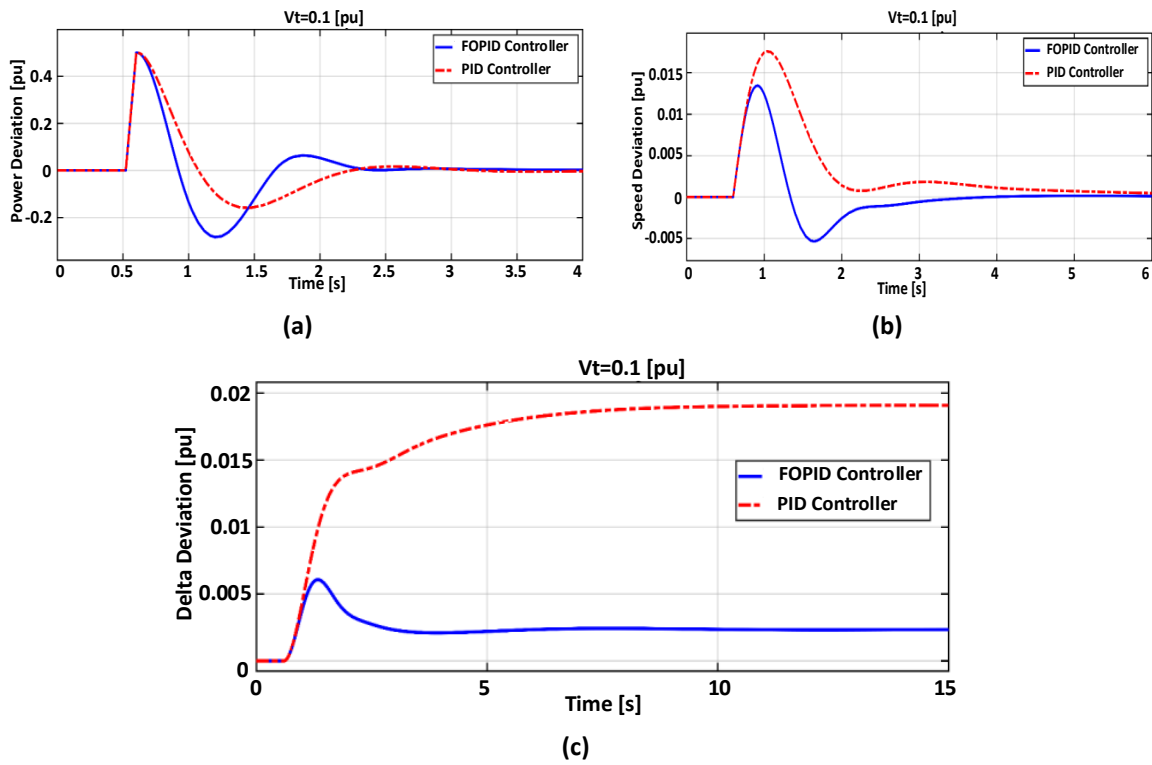

(a)   **(b)**

(c)

Fig. 13. Output signals of the system in scenario 3 by considering $V_t = 0.1$: a) power deviation; b) speed deviation; c) delta deviation.

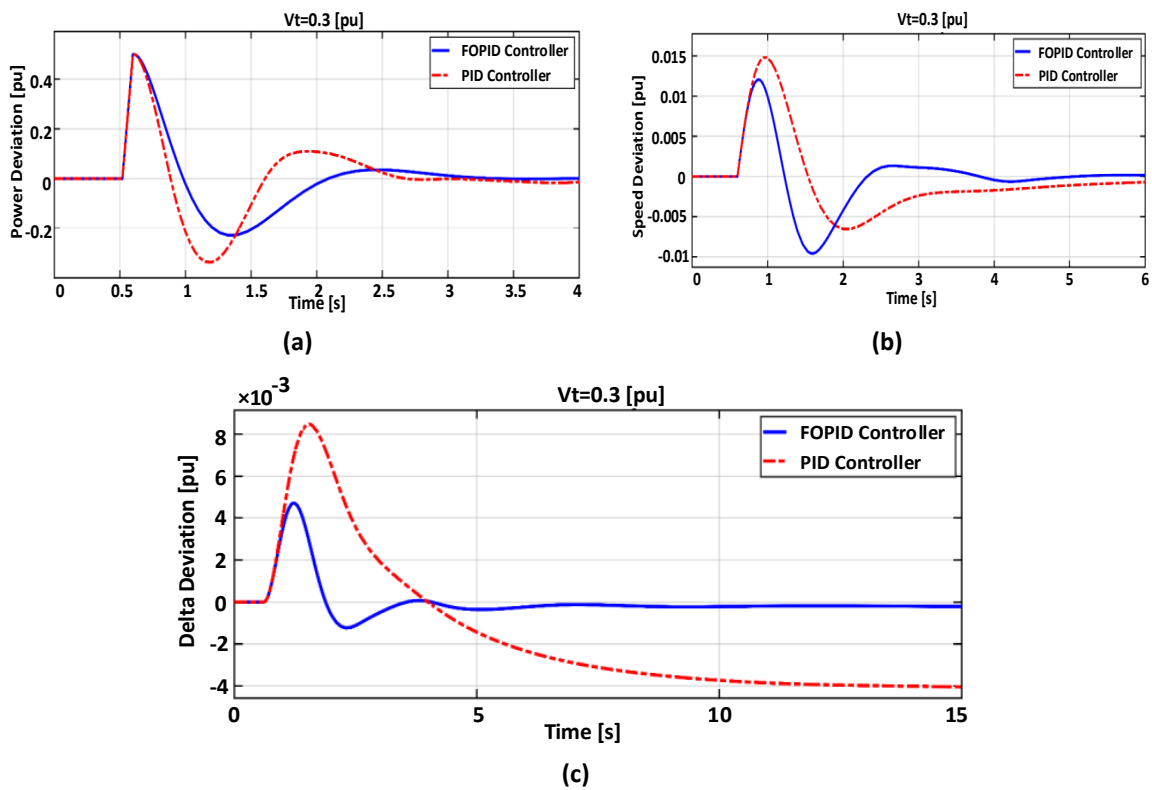**(a)**   **(b)**

(c)

Fig. 14. Output signals of the system in scenario 3 by considering $V_t = 0.3$: a) power deviation; b) speed deviation; c) delta deviation.

5.2. Eigenvalues Analysis

Among the methodologies to evaluate the stability of power system analysis, eigenvalues are one of the most effective methods for finding low-frequency oscillations. Linearizing the system equations around the operating point makes it possible to identify the oscillation modes of the system response. This is achieved by studying the eigenvalues of the system state matrix. Using the system parameters presented in Appendix B, the effective eigenvalues for each scenario are presented in Table 3. In addition, the high-frequency mode is generally considered to be the most sensitive to the electrical dynamics of the stator. The stability of the system can be clearly observed in Fig. 16, as it illustrates the loci of the system's eigenvalues. It is evident that all the eigenvalues have negative real parts, confirming that the system is indeed stable.
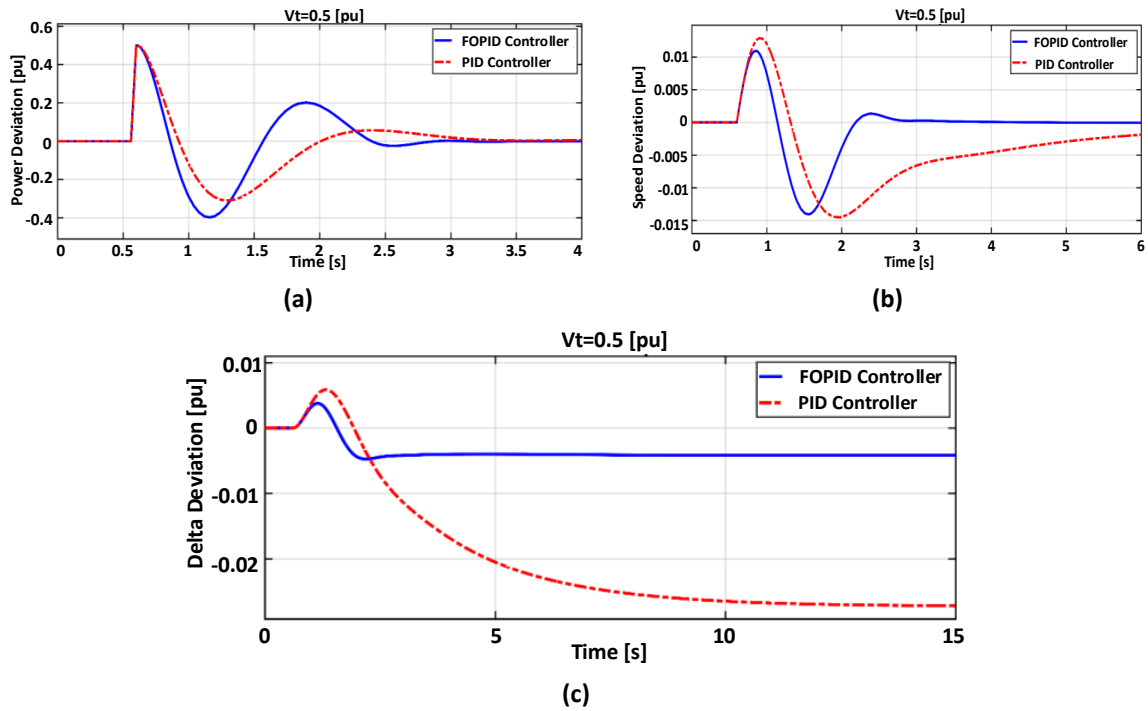

(a)

(b)

(c)

Fig. 15. Output signals of the system in scenario 3 by considering V_t = 0.5: a) power deviation; b) speed deviation; c) delta deviation.
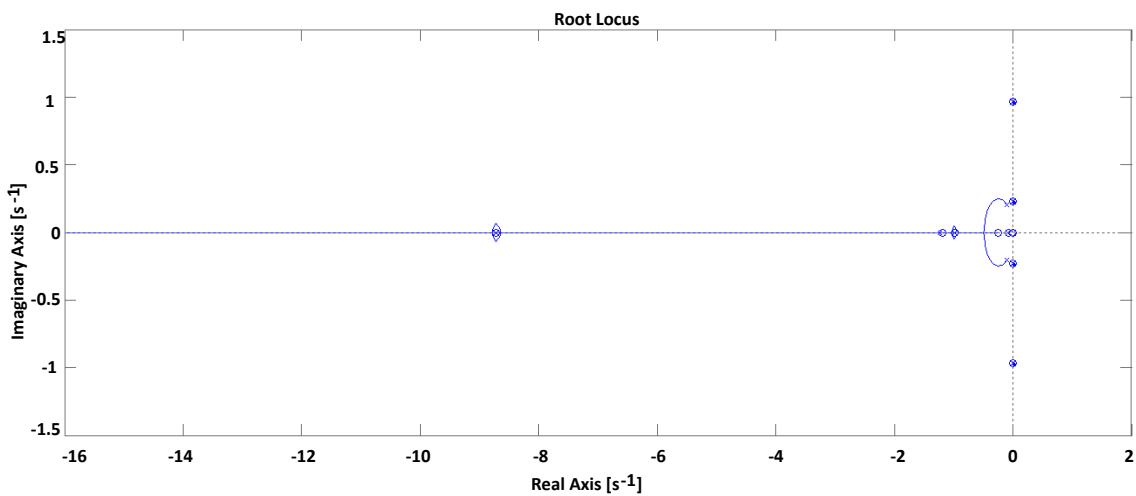

Fig. 16. Loci of eigenvalues of the test system.

5.3. Comparison with the PSO Algorithm

In order to demonstrate the success of the proposed method for designing controllers for the combined SOFC and WT system, it is compared with a PSO algorithm. In Fig. 17, the output signals in the presence of an FOPID controller and using SSA and PSO algorithms are presented. The results show that the parameters of the proposed controller adjusted with the SSA have better results than the PSO algorithm. Therefore, using the SSA to adjust the parameters of the FOPID controller will lead to favorable results in the small signal stability of the system.

Table 3. Eigenvalues analysis for each scenario with the proposed controllers.

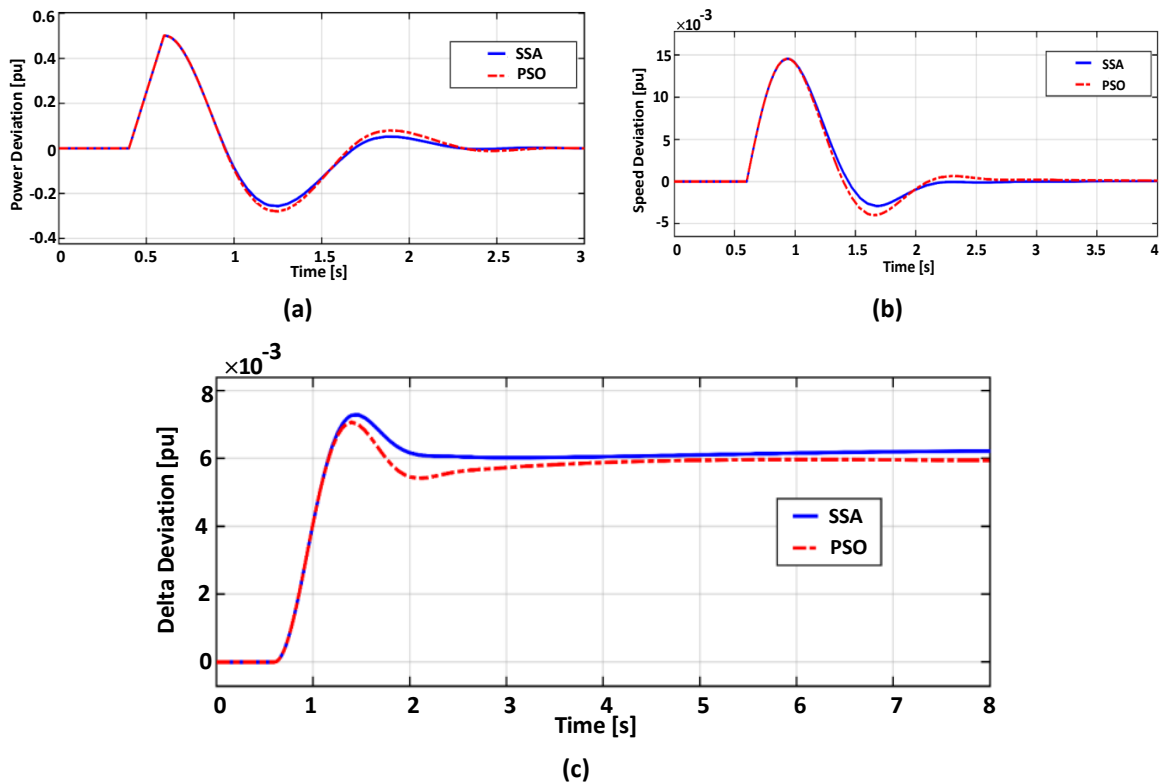| Scenario	PID controller			FOPID controller		
	Eigenvalue	Frequency of oscillations [Hz]	Damping ratio	Eigenvalue	Frequency of oscillations [Hz]	Damping ratio
$x_t = 0.1$	-0.157 ± 2.433i	0.387	0.026	-0.183 ± 2.421i	0.385	0.075
$x_t = 0.5$	-0.103 ± 2.131i	0.339	0.048	-0.147 ± 2.139i	0.340	0.031
$x_t = 1$	-0.142 ± 2.872i	0.457	0.049	-0.176 ± 2.439i	0.388	0.072
$\psi = 30$	-0.059 ± 2.270i	0.361	0.025	-0.063 ± 2.255i	0.359	0.027
$\psi = 70$	-0.069 ± 2.276i	0.362	0.030	-0.084 ± 2.280i	0.363	0.036
$\psi = 100$	-0.086 ± 2.274i	0.362	0.037	-0.108 ± 2.281i	0.363	0.047

Fig. 17. Output signals of the system based on SSA and PSO algorithm: a) power deviation; b) speed deviation; c) delta deviation.

6.   CONCLUSIONS

A mathematical model for a grid-connected MG, which is composed of the SG, WT, and SOFC with the FOPID controller, was proposed. Linearizing the structure of the integrated power system was accomplished by mentioning a routine bus with which three types of power plants are connected. The dynamic behavior of the hybrid system was studied from different angles by using the Heffron-Philips structure, which includes the generation units completely. An optimal FOPID was developed for the hybrid system with the goal of enhancing system stability and damping the oscillations of the power system. The Salp swarm algorithm is exploited to successfully design a robust FOPID damping controller. The proposed approach achieved superb, robust performance for a wide range of operating conditions and disturbances in the presence of the SOFC and WT. The simulation results indicate that the proposed structure is a practical means to improve the stability of the hybrid generation system, which can quickly, and efficiently damp system oscillations and present better performance compared to the PID controller.

APPENDIX A: R_1 AND R_2 OF EQS. (16) AND (17)

$$R_1 = \begin{bmatrix} x_t & x_s + x_t & x_t \\ x_t & x_t & x_t + x_{tw} \\ x_q + x_{ts} + x_t & x_t & x_t \end{bmatrix} , \; R_2 = \begin{bmatrix} x_t & x_s + x_t & x_t \\ x_t & x_t & x_t + x_{tw} \\ x'_d + x_{ts} + x_t & x_t & x_t \end{bmatrix}$$

APPENDIX B: SYSTEM PARAMETERS

Transmission line parameters:

$$X_{ts} = X_t = X_s = X_{tw} = 0.3 \; pu$$

Synchronous machine:

$$X'_d = 0.3 \; pu, \; X_d = 0.3 \; pu, \; X_q = 0.47 \; pu,$$

$$D = 4 \; pu, \; \text{M} = 7.4 \; pu, \; K_a = 10 \; pu, T_a = 0.1 \; s, T'_{d0} = 5 \; s$$

Wind turbine [13]:

$$R_s = 0.0076 \; pu, L_s = 0.171 \; pu, L_m = 2.9 \; pu, \; L_r = 0.156 \; pu, R_r = 0.005 \; pu,$$

$$L_{ss} = L_m + L_s, L_{rr} = L_m + L_r, T'_0 = L_{rr} / R_r, X_s = \omega_s L_{ss}, X'_s = \omega_s \left[L_{ss} - \left(L_m^2 / L_{rr} \right) \right]$$

SOFC:

$$C_{dc} = 1, T_e = 0.08$$

REFERENCES

[1]   P. Thounthong, B. Davat, S. Rael, P. Sethakul, "Fuel cell high-power applications," *IEEE Industrial Electronics Magazine,* vol. 3, no. 1, pp. 32-46, 2009, doi: 10.1109/MIE.2008.930365.

[2]   S. Yu, T. Fernando, T. Chau, H. Iu, "Voltage control strategies for solid oxide fuel cell energy system connected to complex power grids using dynamic state estimation and STATCOM," *IEEE Transactions on Power Systems,* vol. 32, no. 4, pp. 3136-3145, 2017, doi: 10.1109/TPWRS.2016.2615075.

[3]   A. Safari, H. Shahsavari, J. Salehi, "A mathematical model of SOFC power plant for dynamic simulation of multi-machine power systems," *Energy,* vol. 149, pp. 397-413, 2018, doi: 10.1016/j.energy.2018.02.068.

[4]   Y. Li, S. Rajakaruna, S. Choi, "Control of a solid Oxide fuel cell power plant in a grid-connected system," *IEEE Transactions on Energy Conversion,* vol. 22, no. 2, pp. 405-413, 2007, doi: 10.1109/TEC.2005.853756.

[5]   J. Padullés, G. Ault, J. McDonald, "An integrated SOFC plant dynamic model for power systems simulation," *Journal of Power Sources,* vol. 86, no. 1, pp. 495-500, 2000, doi: 10.1016/S0378-7753(99)00430-9.

[6]   Y. Zhu, K. Tomsovic, "Development of models for analyzing the load-following performance of microturbines and fuel cells," *Electric Power Systems Research,* vol. 62, no. 1, pp. 1-11, 2002, doi: 10.1016/S0378-7796(02)00033-0.

[7]   D. Georgakis, S. Papathanassiou, S. Manias, "Modeling and control of a small-scale grid-connected PEM fuel cell system," Proceedings of IEEE Power Electronics Specialists Conference, 2005, doi: 10.1109/PESC.2005.1581846.

[8]   K. Sedghisigarchi, A. Feliachi, "Dynamic and transient analysis of power distribution systems with fuel cells-part I: fuel-cell dynamic model," *IEEE Transactions on Energy Conversion,* vol. 19, no. 2, pp. 423-428, 2004, doi: 10.1109/TEC.2004.827039.

[9]   K. Sedghisigarchi, A. Feliachi, "Dynamic and transient analysis of power distribution systems with fuel cells-part II: control and stability enhancement," *IEEE Transactions on Energy Conversion,* vol. 19, no. 2, pp. 429-434, 2004, doi: 10.1109/TEC.2003.822302.

[10] X. Wu, J. Wang, J. Hao, X. Li, "Control of a solid oxide fuel cell stack based on unmodeled dynamic compensations," *International Journal of Hydrogen Energy,* vol. 43, no. 49, pp. 22500-22510, 2018, doi: 10.1016/j.ijhydene.2018.10.018

[11] A. Safari, A. Badr, M. Farrokhifar, "Modeling of integrated power system with wind turbine based on a doubly fed induction generator and solid oxide fuel cell for small-signal stability analysis," *International Transactions on Electrical Energy Systems,* vol. 29, no. 11, 2019, doi: 10.1002/2050-7038.12119.

[12] S. Chatterjee, A. Naithani, V. Mukherjee, "Small-signal stability analysis of DFIG based wind power system using teaching learning-based optimization," *International Journal of Electrical Power & Energy Systems,* vol. 78, pp. 672-689, 2016, doi: 10.1016/j.ijepes.2015.11.113.

[13] F. Wu, X. Zhang, K. Godfrey, P. Ju, "Small signal stability analysis and optimal control of a wind turbine with doubly fed induction generator," *IET Generation, Transmission, Distribution*, vol. 1, no. 5, pp. 751-760, 2007, doi: 10.1049/iet-gtd:20060395.

[14] M. Zamanifar, B. Fani, M. Golshan, H. Karshenas, "Dynamic modeling and optimal control of DFIG wind energy systems using DFT and NSGA-II," *Electric Power Systems Research,* vol. 108, pp. 50-58, 2014, doi: 10.1016/j.epsr.2013.10.021.

[15] H. Geng, X. Xi, G. Yang, "Small-signal stability of power system integrated with ancillary-controlled large-scale DFIG-based wind farm," *IET Renewable Power Generation,* vol. 11, no. 8, pp. 1191-1198, 2017, doi: 10.1049/iet-rpg.2016.0078.

[16] M. Shahriar, M. Shafiullah, M. Rana, "Stability enhancement of PSS-UPFC installed power system by support vector regression," *Electrical Engineering,* vol. 100, no. 3, pp. 1601-1612, 2018, doi: 10.1007/s00202-017-0638-8.

[17] W. Gil-González, O. Montoya, "Passivity-based PI control of a SMES system to support power in electrical grids: A bilinear approach," *Journal of Energy Storage,* vol. 18, pp. 459-466, 2018, doi: 10.1016/j.est.2018.05.020.

[18] E. Kabalci, "Design and analysis of a hybrid renewable energy plant with solar and wind power," *Energy Conversion and Management,* vol. 72, pp. 51-59, 2013, doi: 10.1016/j.enconman.2012.08.027.

[19] K. Rajesh, A. Kulkarni, T. Ananthapadmanabha, "Modeling and simulation of solar PV and DFIG based wind hybrid system," *Procedia Technology,* vol. 21, pp. 667-675, 2015, doi: 10.1016/j.protcy.2015.10.080.

[20] M. Iqbal, "Modeling and control of a wind fuel cell hybrid energy system," *Renewable Energy,* vol. 28, no. 2, pp. 223-237, 2003, doi: 10.1016/S0960-1481(02)00016-2.

[21] M. Khan, M. Iqbal, "Dynamic modeling and simulation of a small wind–fuel cell hybrid energy system," *Renewable Energy,* vol. 30, no. 3, pp. 421-439, 2005, doi: 10.1016/j.renene.2004.05.013.

[22] N. Bizon, "Optimal operation of fuel cell/wind turbine hybrid power system under turbulent wind and variable load," *Applied Energy,* vol. 212, pp. 196-209, 2018, doi: 10.1016/j.apenergy.2017.12.034.

[23] S. Chuang, C. Hong, C. Chen, "Design of intelligent control for stabilization of microgrid system," *International Journal of Electrical Power & Energy Systems,* vol. 82, pp. 569-578, 2016, doi: 10.1016/j.ijepes.2016.04.030.

[24] R. Amini, A. Safari, S. Ravadanegh, "Optimal model of PDIG based microgrid and design of complementary stabilizer using ICA," *ISA Transactions,* vol. 64, pp. 328-341, 2016, doi: 10.1016/j.isatra.2016.04.010.

[25] H. Shahsavari, A. Safari, J. Salehi, "Dynamic analysis and optimal design of FLPSS for power network connected solid oxide fuel cell using of PSO," *Journal of Operation and Automation in Power Engineering,* vol. 5, no. 2, pp. 215-225, 2017, doi: 10.22098/joape.2017.3563.1282.

[26] Y. Jia, T. Huang, Y. Li, R. Ma, "Parameter setting strategy for the controller of the DFIG wind turbine considering the small-signal stability of power grids," *IEEE Access,* vol. 8, pp. 31287-31294, 2020, doi: 10.1109/ACCESS.2020.2973281.

[27] S. Essallah, A. Bouallegue, A. Khedher, "Integration of automatic voltage regulator and power system stabilizer: small-signal stability in DFIG-based wind farms," *Journal of Modern Power Systems and Clean Energy,* vol. 7, no. 5, pp. 1115-1128, 2019, doi: 10.1007/s40565-019-0539-0.

[28] H. Guo, W. Gu, M. Khayatnezhad, N. Ghadimi, "Parameter extraction of the SOFC mathematical model based on fractional order version of dragonfly algorithm," *International Journal of Hydrogen Energy,* vol. 47, no. 57, pp. 24059-24068, 2022, doi: 10.1016/j.ijhydene.2022.05.190.

[29] J. Huang, Z. Yang, J. Yu, J. Liu, Y. Xu, X. Wang, "Optimization for DFIG fast frequency response with small-signal stability constraint," *IEEE Transactions on Energy Conversion,* vol. 36, no. 3, pp. 2452-2462, 2021, doi: 10.1109/TEC.2021.3051944.

[30] Y. Zhou, Q. Hua, P. Liu, L. Sun, "Multi-objective optimal droop control of solid oxide fuel cell based integrated energy system," *International Journal of Hydrogen Energy,* vol. 48, no. 30, pp. 11382-11389, 2023, doi: 10.1016/j.ijhydene.2022.04.071.

[31] J. Yang, Y. Chen, Y. Hsu, "Small-signal stability analysis and particle swarm optimisation self-tuning frequency control for an islanding system with DFIG wind farm," *IET Generation, Transmission & Distribution*, vol. 13, no. 4, pp. 563-574, 2018, doi: 10.1049/iet-gtd.2018.6101.

[32] X. Fang, J. Yao, R. Liu, Y. Zhao, P. Sun, S. Huang, "Small-signal stability analysis and current control reference optimization algorithm of DFIG-based WT during asymmetric grid faults," *IEEE Transactions on Power Electronics,* vol. 36, no. 7, pp. 7750-7768, 2021, doi: 10.1109/TPEL.2020.3042514.

[33] A. Ahmed, M. Shahid Ullah, M. Hoque, "Optimal design of proportional–integral vontrollers for grid-connected solid oxide fuel cell power plant employing differential evolution algorithm," *Iranian Journal of Science and Technology, Transactions of Electrical Engineering,* vol. 43, no. 4, pp. 999-1019, 2019, doi: 10.1007/s40998-019-00207-5.

[34] S. Mirjalili, A. Gandomi, S. Mirjalili, S. Saremi, H. Faris, S. Mirjalili, "Salp swarm algorithm: A bio-inspired optimizer for engineering design problems," *Advances in Engineering Software,* vol. 114, pp. 163-191, 2017, doi: 10.1016/j.advengsoft.2017.07.002.

[35] P. Kundur, *Power System Stability and Control*, New York: McGraw-Hill, 1994.

[36] L. Yazhou, A. Mullane, G. Lightbody, R. Yacamini, "Modeling of the wind turbine with a doubly fed induction generator for grid integration studies," *IEEE Transactions on Energy Conversion,* vol. 21, no. 1, pp. 257-264, 2006, doi: 10.1109/TEC.2005.847958.

[37] Y. Ku, "Electric Power System Dynamics," New York: McGraw-Hill, 1983.

[38] B. Hekimoglu, "Optimal tuning of fractional order PID controller for DC motor speed control via chaotic atom search optimization algorithm", *IEEE Access,* vol. 7, pp. 38100-38114, 2019, doi: 10.1109/ACCESS.2019.2905961.

[39] H. Shahsavari, A. Nateghi, "Optimal design of probabilistically robust $PI^\lambda D^\mu$ controller to improve small signal stability of PV integrated power system, " *Journal of the Franklin Institute*, vol. 356, no. 13, pp. 7183-7209, 2019, doi: 10.1016/j.jfranklin.2019.03.035.